Flow-induced Crystallization of Long Chain Aliphatic Polyamides under a Complex Flow Field: Inverted Anisotropic Structure and Formation Mechanism

Yunyun Gao[a], Xia Dong[a,]*, Lili Wang[a], Guoming Liu[a], Xianggui Liu[a], Cristina Tuinea-Bobe[b], Ben Whiteside[b], Phil Coates[b], Dujin Wang[a] , Charles C. Han[a]

[a]*Beijing National Laboratory for Molecular Sciences, CAS Key Laboratory of Engineering Plastics, Institute of Chemistry, Chinese Academy of Sciences, Beijing 100190, China*

[b]*Polymer IRC, University of Bradford, Bradford BD71DP, UK*

***** Corresponding author: X. Dong (xiadong@iccas.ac.cn)

Abstract

The present work deals with the flow-induced multiple orientations and crystallization structure of polymer melts under a complex flow field. This complex flow field is characteristic of the consistent coupling of extensional "pulse" and closely followed shear flow in a narrow channel. Utilizing an ingenious combination of an advanced micro-injection device and long chain aliphatic polyamides (LCPA), the flow-induced crystallization morphology was well preserved for ex-situ

synchrotron micro-focused wide angle X-ray scattering (μWAXS) as well as small angle X-ray scattering (SAXS). An inverted anisotropic crystallization structure was observed in two directions: perpendicular and parallel to the flow direction (FD). The novel anisotropic morphology implies the occurrence of wall slip and "global" fountain flow under the complex flow field. The mechanism of structure formation is elucidated in detail. The experimental results clearly indicate that the effect of extensional pulse on the polymer melt is restrained and further diminished due to either the transverse tumble of fountain flow or the rapid retraction of stretched high molecular weight tails. However, the residual shish-kebab structures in the core layer of the far-end of channel suggest that the effect of extensional pulse should be considered in the small-scaled geometries or under the high strain rate condition.

1. Introduction

Flow-induced crystallization (FIC) of polymer melts is a fundamental issue of polymer physics. It is of clear theoretical significance, and very important in practical applications. Developing specific flow condition by using delicate flow geometries is an important method through which the cause-effect relationship among polymer-surface interactions, melt flow behavior and subsequent crystallization can be investigated. However, most studies of experimental protocols reported in these literatures involve only shear [1-8] or extensional flow [9-13], rather than complex flow field. The main reason might be perceived experimental difficulties and a lack of

correlation between molecular orientation and non-Newtonian flow behavior under complex flow field. Although computer simulations provide many valuable information of system on a macroscopic scale [14], i.e. flow pattern, viscosity, stress profile, etc., there is still the need for probing the microscopic picture of flow behavior under complex flow field as well as its effect on crystallization of polymers.

One of the most prominent industrial flow field is the consistent coupling of extensional "pulse" and closely following shear flow. For example, in injection-moulding processes, polymer melts usually experience short-term extensional effect caused by converging flow at the sprue entrance, then flow rapidly into the rather colder mould and solidify while subjected wall shear stress. Early experiments suggested that the transient extensional effect is important during the very early stage before the fully development of laminar shear flow [15]. Nevertheless, most researchers tend to consider that the FIC in filling channel is dominated by shear effect solely. While in some cases, the effect of so-called fountain flow, a two dimensional flow restricted to a small region of the flow front, is also suggested [16-18]. However, several phenomena in this widespread process have not been sufficiently recognized. First, if one wants to reproduce the condition that polymer experience during the industrial processes, how to deal with the non-isothermal nature of those complex flow geometries, especially the temperature gradient between two flow patterns, will become a very delicate task. Second, if converging flow is

generally referred to as a “strong” flow, which would generate considerable chain stretching conditions [19, 20], then why its contribution is not being valued. Indeed, the relaxation of oriented or stretched polymer chains might not allow the effect of extensional pulse to be observed in the final products. However, nowadays, the desire for high productivity in the industry makes the strain rate of processing grow by leaps and bounds. The effect of extensional pulse might not keep invisible anymore. Third, as the demand of micro or sub-micro components is rising rapidly, it is very necessary to consider the potential deviation of flow behavior from the typical shear field in those small-scaled geometries.

To explore the crystallization of polymer melt in the extensional-shear-coupled flow filed, a simple case is studied in this work. Through a short entrance polymer melts are jetted into a thin and straight-walled channel, and subsequently crystallize under wall shear stress. An advanced micro-injection device was employed as a protocol to introduce this complex flow field. By applying the sprue-less design, the injection nozzle is in direct contact with a thin cavity. Flow visualization techniques showed that the transient extensional pulse occurs as the converging flow at the junction between the nozzle and the cavity, while the shear flow closely follows in the rest part of cavity [22]. As the cavity size decreases, several effects are promoted to help further understand FIC behavior under the complex flow field [21, 22]: (i) a considerably high strain rates can be imposed to secure the strong chain stretching

79 condition; (ii) the heat transfer becomes more efficient, thus an isothermal condition
80 can be applied on the shear pureion; (iii) converging flow and shear flow are strongly
81 coupled, since there is no room for radical free-surface flow (i.e. flow with zero
82 lateral-stress).

83 Another question is the applicable polymer system. To deal with the non-isothermal
84 condition, it is very important to use a polymer which can respond quickly to the
85 processing history it experiences. To preserve the effect of flow condition, it should
86 also have rather slow relaxation dynamics. In addition, the chain stretching condition
87 of this polymer should be able to be quantitatively described. Based on those
88 considerations, long chain aliphatic polyamides (LCPA) are introduced. By
89 incorporating long alkane segments − typically more than ten methylene groups and
90 hence diluting the amide linkages, LCPA serve as the example of a polymer
91 possessing intrinsic flexibility and strong intermolecular interaction simultaneously
92 [23]. Generally, at temperatures well above the melting point, the hydrogen bonds
93 between the molecules of LCPA are weakened (both in terms of individual bond
94 strength and total number), which leads to the exhibition of flexibility. Rheological
95 models, such as the Doi-Edwards model, are applicable in this case. On the other side,
96 when LCPA are cooled back towards the melting point, the strong chain interaction
97 reconstructs again to affect the relaxation behavior and, most importantly, fasten
98 crystallization dynamics [24]. The efficient heat transfer of experimental protocols

and special feature of LCPA could result in well-recorded crystallization morphology. Hence, it is possible and convenient to ex-situ probe the flow-induced hierarchical crystallization structure. In this work, synchrotron micro-focused wide angle X-ray scattering (μWAXS) as well as small-angle X-ray scattering (SAXS) were used. The microscopic morphology can be spatially resolved directly using high-resolution scanning diffractometry of μWAXS [25, 26]. Those methods require little sample preparation and thus diminish the risk of introducing artifacts [26, 27]. In combination with vastly exiting information, FIC behavior under complex flow field can be understand more thoroughly.

2. Experimental

2.1 Materials and sample preparation

The additive-free PA1012 was produced from bio-fermenting sources (Shandong Guangyin New Materials Co. Ltd, Zibo, China). The melting point was 189 ℃ determined by differential scanning calorimeter with heating rate of 10 ℃/min. The melt flow index was 0.72 g/10min at 235 ℃ using 2.16 kg as loading. Since PA1012 has very similar molecular structure and physics properties to PA1212, the weight-average molecular weight ($\bar{M}_w$) of PA1012 was thus characterized by the empirical equation $[\eta] = 6.54\times10^{-2}\bar{M}_w^{0.70}$ for polyamide 1212 as reference. The molecular weight $\bar{M}_w$ of PA1012 was 265 kg/mol, where the intrinsic viscosity ($[\eta]$)

was 409.3 mL/g using m-cresol as the solvent. The molecular chain length of PA1012 with this $\bar{M}_w$ is long enough to form ordering structures.

Fig. 1 shows how temperature exercises influence upon the relaxation behavior of PA1012 melts. At short relaxation times, $G(t)$ changes little in a broad temperature range, which indicates the global configuration of the chain as well as stiffness of a single chain is less affected at temperature above the melting temperature, $T_{m.}$ While at long times, $G(t)$ is explored into the terminal relaxation regime above 230 ºC but into the plateau regime at 210 ºC and 190 ºC. The reconstruction and strength increase of hydrogen bonding at lower temperature give rise to a sudden leap of physical entanglement points leading to the slow relaxation dynamics of large motion units.

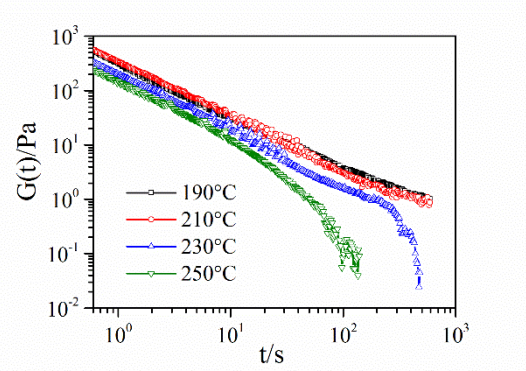

Fig. 1. Apparent stress relaxation modulus, $G(t) = \sigma(t)/\gamma$, plotted logarithmically against time for PA1012 at different temperature. The value of strain γ is 10% for all experiments.

The sprue-less micro-injection moulding device (Battenfeld Microsystem 50) was used to create the complex extensional-shear-coupled flow filed. The diameter of the nozzle was 5 mm. The dimension of followed straight-wall channel was 20.0×1.5×0.5

135 mm^3 (length direction (LD) × width direction (WD) × thickness direction (TD)).
136 Converging flow occurred at the junction between nozzle and cavity. Fig. 2 shows the
137 sample for ex-situ investigation and the sites of the flow types adapted from
138 computational fluid dynamics simulation result [22]. The color of sample represents
139 the time scale of arrival flow front. The cavity temperature was set as 80 ℃ attaining
140 balance between processability and slow relaxation dynamics. The injection rate was
141 100 mm/s. The whole mould filling process would be finished within sub-0.1s. This
142 short processing time scale suggests the mould filling procedure is ahead of the
143 complete solidification of PA1012 at the moulding temperature. The material was
144 melted at 270 ℃ initially by a rotating screw positioned at a 45 °angle. It was pushed
145 by the screw in a very accurate metering chamber. Then, the injection piston jetted the
146 material through the barrel (270 ℃) and the sprue-less nozzle (250 ℃) into the cavity.
147 Highly repeatable process control and accurate material dosing were observed during
148 moulding by monitoring shot to shot variation of dosing performance and pressure
149 curves. PA1012 granules were kept in a vacuum oven at 80 ℃ for 24 h for drying
150 before preparation.

151 *2.2 Micro-focus wide angle X-ray scattering scanning*

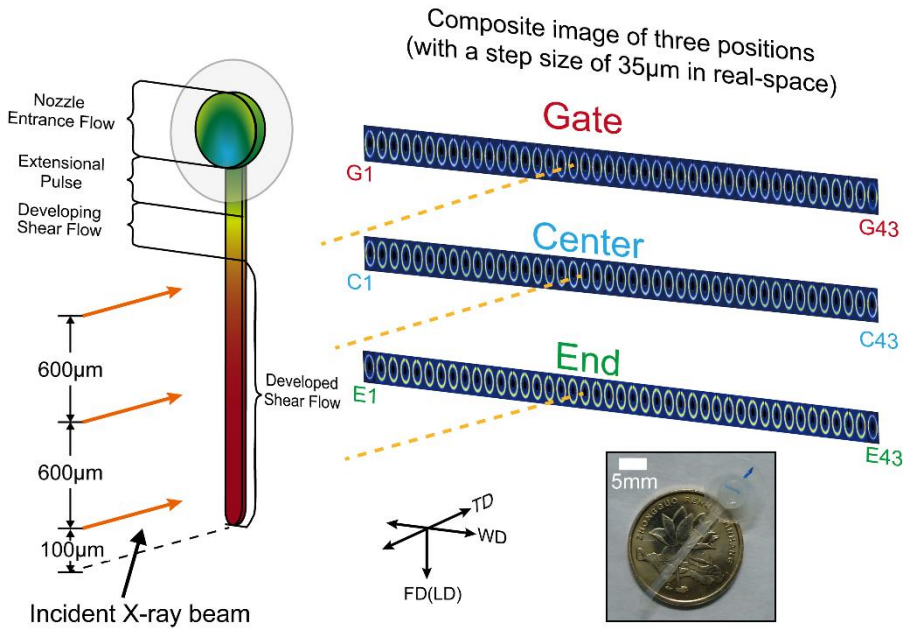

Fig. 2. Sample for ex-situ probing and the supposed site of the flow types. The scheme of experimental geometry shows the procedure of μWAXS scanning and resultant diffraction patterns (thumbnails). Insert: the actual plaque-shaped sample.

The X-ray source for diffractometry was BL15U, the hard X-ray micro-focused beamline at SSRF (Shanghai Synchrotron Radiation Facility). Using a Si/Rh coated K-B mirror-pair, the beam was focused on the sample with a 3×3 μm^2 beam size at focal position. The sample was mounted on a three-axis motorized translation stage. A standardized line scanning program with the X-ray beam perpendicular to the WD-LD plane was carried out at three different equidistant positions (Fig. 2) marked as 'gate', 'center' and 'end' to investigate the crystal structure and orientation changes both perpendicular and parallel to the flow direction (FD). The distance between the end position and the far-end of sample was 100 μm. The step size between each adjacent focus spot was 35 μm hence 43 individual diffraction patterns obained at Gate, Center

and End positions separately. Data was collected using a MARCCD detector with an average pixel size of 79×79 μm^2. The photon energy was 18 KeV giving a wavelength of 0.688 Å with the sample-to-detector distance of 206.3 mm. The exposure time was 1 s. Each diffraction pattern frame was denominated using the initials of scan position plus the number of scan sequence at this position, i.e., frame 1 at gate position would be G1, frame 2 at center position C2, frame 3 at end position E3, etc. Background reduction and automated batch-operation of μWAXS patterns were conducted using the Fit2D software package. Self-designed Matlab programs were used to give pattern visualization and plotting.

The phase content for internal comparison within the batches is presented as crystallinity index (χ_c):

$$\chi_c = \frac{A_c}{\sum A_c + A_A} \qquad (1)$$

where A_c is the integrated area of crystalline peaks belonging to a specific crystal phase and A_A is the integrated area of amorphous halo.

The peak deconvolution was performed with the constraint conditions (see **Supporting Information**) and these constraint conditions were necessary to determine the center of amorphous halo and each reflection separately because the amorphous halo and multiple phase signals were combined together in the origin testing data. To fulfill the description of the whole orientation state, the approach

185 derived from Wu and Schultz's [28] was adopted to quantify the mesophase contents.

186 The percentage of the mesophase (P_{meso}) can be calculated as:

187 $$P_{meso} = POP - \sum \chi_c \qquad (2)$$

188 $$POP = \frac{\int_0^{2\pi} [\int_S I(s,\phi)ds - I_b(\phi)]d\phi}{\int_0^{2\pi} \int_S I(s,\phi)dsd\phi} \qquad (3)$$

189 where POP is the percentage of oriented phases; s is the scattering vector; ϕ is the
190 azimuthal angle; $I(s,\phi)$ is the background-corrected intensity from the diffraction
191 pattern; $I_b(\phi)$ is the baseline of the azimuthal intensity profile resulted solely from the
192 integral over a domain S of $I(s,\phi)$, herein S is as the same scattering angular range as
193 the one used in calculating χ_c.

194 To manifestly demonstrate the crystallization structure, as shown in Fig. 3, the
195 xy-coordinate pattern is transformed to polar coordinates with the scattering angle
196 ranging from 8.0 ºto 11.4 ºand the azimuthal angle from 0 to 360 º.

197 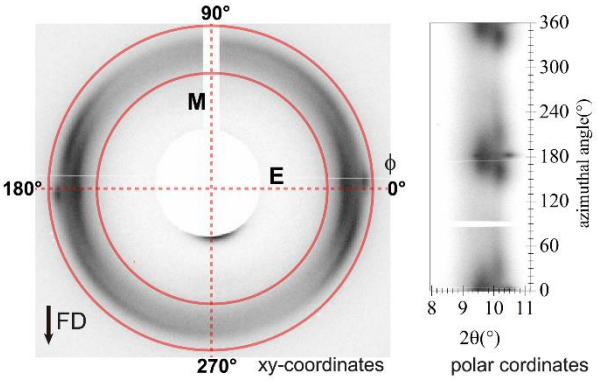

198 **Fig. 3.** Demonstration of the regions used for generating the polar coordinate pattern
199 from the xy-coordinate pattern. E and M represent the equatorial and meridian
200 direction, respectively. The definition of azimuthal angle are also shown.

2.3 Small angle X-ray scattering

SAXS data at gate, center and end position were collected on the BL16B beamline of SSRF. To mitigate against a resolution problem from simultaneous scattering from two different highly oriented layers, the skin layer was blocked (sides) or cut away (top/bottom) deliberately in the SAXS experiments. The focus spot size was 0.3×0.2 mm^2. A radiation wavelength of 1.24Å was applied with the data collected using the same type of MARCCD detector as used for the BL15U experiment. Two different sample-to-detector distances, 2074.7 mm and 5088.6 mm, were employed to explore lamellae reflection and central diffuse scattering signal, respectively. The exposure time was 60s and 20s, respectively. According to the reciprocal relationship in scattering, the central diffuse scattering signal from fibrils or shishes would be much larger and more intense in the case of long s-d distance. Thus, to avoid overexposure, shorter exposure time was used for longer s-d distance. In addition, the high vacuum optical path in BL16B ensures that the atmospheric scattering in both cases is greatly eliminated. All SAXS patterns were corrected for background and X-ray fluctuation. To obtain the 1D scattering profile, $q=4\pi(\sin\theta)/\lambda$ was used, where q is the module of scattering vector; θ is one half the scattering angle; λ is the X-ray wavelength.

3. Results and Discussion

3.1 Determining flow regime of extensional pulse.

220 The dimensionless group Weissenberg number (*Wi*) is used to rheology characterize
221 the strength of extensional pulse due to converging flow. In the case of extensional
222 flow at channel entry, two *Wi* related to two different time scale can be expressed as
223 [19, 29]:

224 $$Wi, \mathrm{rep} = \tau_{\mathrm{rep}} \ln\left[\left(\frac{R_O}{R_C}\right)^2\right]\left(\frac{4Q}{\pi R_C^3}\right) \quad (4)$$

225 $$Wi, \mathrm{s} = \tau_s \ln\left[\left(\frac{R_O}{R_C}\right)^2\right]\left(\frac{4Q}{\pi R_C^3}\right) \quad (5)$$

226 where τ_{rep} is the reptation time; τ_s is the time scale for faster chain retraction (Rouse
227 relaxation time); R_O is the radius of nozzle; R_C is the equivalent radius of cavity and
228 the R_C of cavity is 0.455 mm calculated from Huebscher equation.; Q is the
229 volumetric flow rate. The largest reptation time for high molecular weight (HMW)
230 tails, $\tau_{\mathrm{rep}}^{\mathrm{HMW}}$,is the proper choice for τ_{rep} due to the crucial role of them in forming
231 oriented structure [9, 19, 30] and is estimated as 6s at 250 ºC from the relaxation time
232 spectrum (see **Supporting Information**). According to Doi−Edwards theory [31], the
233 relation between above two relaxation time is $\tau_s = \tau_{\mathrm{rep}}^{\mathrm{HMW}}/3Z$, where Z is the average
234 number of entanglements and $Z = M_w/M_e$. The molecular mass between
235 entanglements M_e, calculated from $M_e = \rho RT / G_N^0$, is 21.7 kg/mol for PA1012 at 250
236 ºC, resulting in a Z value of 12. For the rheological description, τ_{rep} and τ_s are regarded
237 as orientation relaxation time and stretch relaxation time, respectively. In the flow
238 regime Wi,rep, Wi,s > 1, a strain rate greater than $1/\tau_{\mathrm{rep}}$ and $1/\tau_s$ indicates the fast flow

239 condition. As a result, chain sections are strongly oriented and the chain conformation
240 becomes similar to that of the crystalline state. The calculated magnitude of *Wi*,rep is
241 about 5.43×10^5. Such a large magnitude of *Wi*,rep guarantees the strong oriented
242 courter path of polymer chains. Moreover, the magnitude of *Wi*,s following from τ_s is
243 considerably larger than 1 (1.51×10^4), suggesting the polymer chain of HMW is
244 strongly stretched. Hence, the strong extensional flow at nozzle entrance and relative
245 low entanglement density ensure the sufficient stretch of the polymer chains or chain
246 sections to fulfil the formation of oriented nuclei. It is also noticed that the calculated
247 Z value is comparable to the simulation result $Z \leqslant 10$ for which the G(t) shows no
248 sign of plateau regime [32]. This is reconciled with the rheology data at 250 °C and
249 thus confirms the reliability of calculation of *Wi*,s.

250 *3.2 Analysis of crystallization structure*

251 Fig. 4a shows the first frame collected at the gate position (G1). This diffraction
252 pattern is similar to that found in highly oriented polyamide samples [33]. The major
253 difference between this pattern and the one of common highly oriented polyamide is
254 the distinguishable coexistence of α-phase and β-phase crystals in the present case.
255 Two signals superposed at the inner layer ($2\theta = 9.11$ °) are contributed from the
256 diffraction of both α100 and β100 planes. Another two signals emerging at outer
257 layers ($2\theta = 9.95$ °and 10.43 °, respectively) can be indexed to α010/110 and β020/120
258 planes, respectively. Since the diffraction arcs are not fully separated, the β-phase is

259 inferred from the relatively greater outer arcing due to the presence of β020/120
260 diffraction signals [35]. In addition, it can be observed that the reflection maximum
261 shifts about 7 degree from the equatorial.

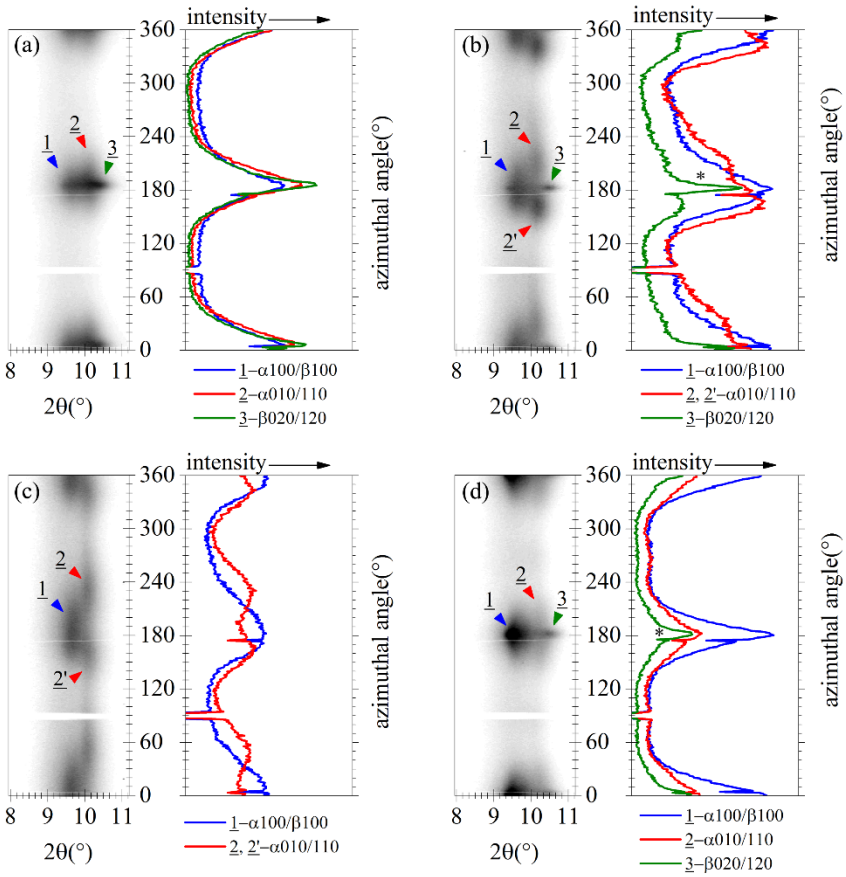

262

263 **Fig. 4.** The wide angle X-ray reflection signals at (a) G1; (b) G2; (c) G3 and (d) G10
264 in polar coordinates. The graphics to the right represent the corresponding azimuthal
265 intensity profiles. The colored arrows indicate the specific reflection. The β020/120
266 profiles marked * inevitably overlap with α010/110 profiles. Oriented β-phase can be
267 observed from the peak around 180 º.

268 Next to the G1, G2 (Fig. 4b) shows that the α010/110 planes superposed in G1 have
269 separated into four off-equatorial and intensity-unequal arcs. This pattern formation

nevertheless results from, statistically, precessional rotation of uniaxial oriented crystals. The peak position of α010 is split by ±30 °and the α110 by ±18 ° about the equator. Using the unit cell for α-phase of PA1012 reported by Jones *et al*. [36] (a=0.459 nm, b=0.530 nm, c=2.98 nm, α=50º, β=77º, γ=64º), the ideal reciprocal space angles in the X-ray diffraction patterns from lamellar-crystal mats (taken with X-ray beam parallel to the lamellae surface) can be concluded as follows: the 100 should be split by ±5 °, the 010 by ±38 ° and the 110 by ±33 ° about the either side of equator. The implication of this difference, according to Dreyfuss and Keller's observation in polyamide 66, 610 and 612, accounts for the partial randomization around the a-axis [37]. Because the a-axis is the direction of hydrogen bond progression corresponding with the fastest crystal growth, this pattern is favorably consistent with the structure of α-phase crystals as the incomplete twisting chain-fold lamellae [1, 38]. The separation of α010/110 reflections also makes the shadowed β020/120 signals more apparent in G2. Although the α-phase crystals lose orientation uniformity in at least in one direction, it seems that the orientation state of β-phase remains unchanged.

G3 (Fig. 4c) shows very different formations. Two strong peaks at the equatorial are characteristic of β-phases present in both G1 and G2. However, in G3, sharp peaks cannot be found either from the inner layer or from the outer layers, which indicates that there is no β-phase present at this location. Moreover, the disorientation of the

α-phase can be observed from the relative larger spreads, particularly along the α100 arcs. Comparing to X-ray diffraction patterns from lamellar-crystal mats, the intensity differences of α-phase signals (unequal arcs) also indicate the incomplete twisting of lamellae.

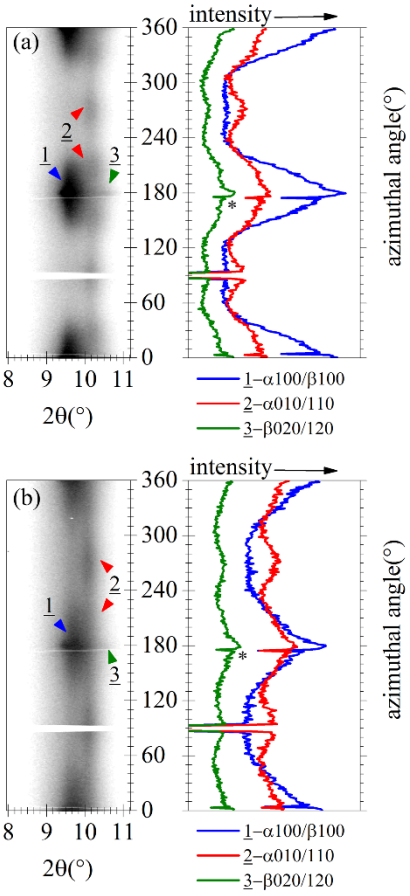

Fig. 5. The wide angle X-ray reflection signals at (a) C22; (b) E22 and their intensity profiles. Colored arrows indicate the specific reflection. The β020/120 profiles marked * have the same meaning with those in Fig. 4.

The β-phase crystals can be seen again at G8 located at about 245 μm from the edge of the sample and is present up to G38, which is located at almost the same distance from the opposite edge. Between those two frames, the diffraction patterns clearly

present a superposition of arcs from the α-phase and sharp equatorial reflections from the β-phase, as presented in Fig. 4d, and indicates that while both α-phase and β-phase crystals are uniaxial oriented the β-phase exhibits a more highly oriented state.

Crystallization structure changes within the WD at the center and end positions follow similar rules to those seen at the gate position. However, the strong meridian signals found in around the centerline of above two positions, such as C22 and E22 (Fig. 5), are clear enough to indicate the evolution tendency of the flow field along the FD. Since the azimuthal intensity distributions of the α100 reflections and the β100 reflections in samples C22 and E22 remain comparatively unchanged compared to G8, the appearance of the meridian signals cannot be simply interpreted as the ensemble rotation of crystals, but should be still considered as a consequence from a random orientation about the a-axis [1]. If the X-ray is vertical to the fiber axis, a uniformly twisting lamellae, which is equivalent to a completely random state around the a-axis, would generate a pattern with α010 reflections center on the meridian with spreads decreasing towards the equatorial and the α110 has the maxima between the meridian and equatorial with decreasing intensity to each direction [37]. Nevertheless the α100 reflection should be less affected by this twisting structure. Similar oriented and twisting texture for α-phase crystals of polyamides can be found in some spherulites [34] and the transcrystallites growing epitaxially on fibers [39]. In addition, given that

β-phase crystals are highly oriented in both cases, the most possible morphology represented by C22 and E22 is that α-phase crystals, in a complete twisting mode, epitaxially grew on the long-range ordered β-phase crystals.

3.3 Analysis of anisotropic structure

The so-called skin-core morphology, an anisotropy perpendicular to the FD, is a typical inhomogeneous structure resulted by different regimes of shear flow [19, 40]. Fig. 5 shows the normalized azimuthal intensity scans of different reflections at three positions. The profile data are plotted to a color scale image with full azimuthal angle as the x-axis and real-space scan position as the y-axis. On this basis, three distinct structural layers are identified.

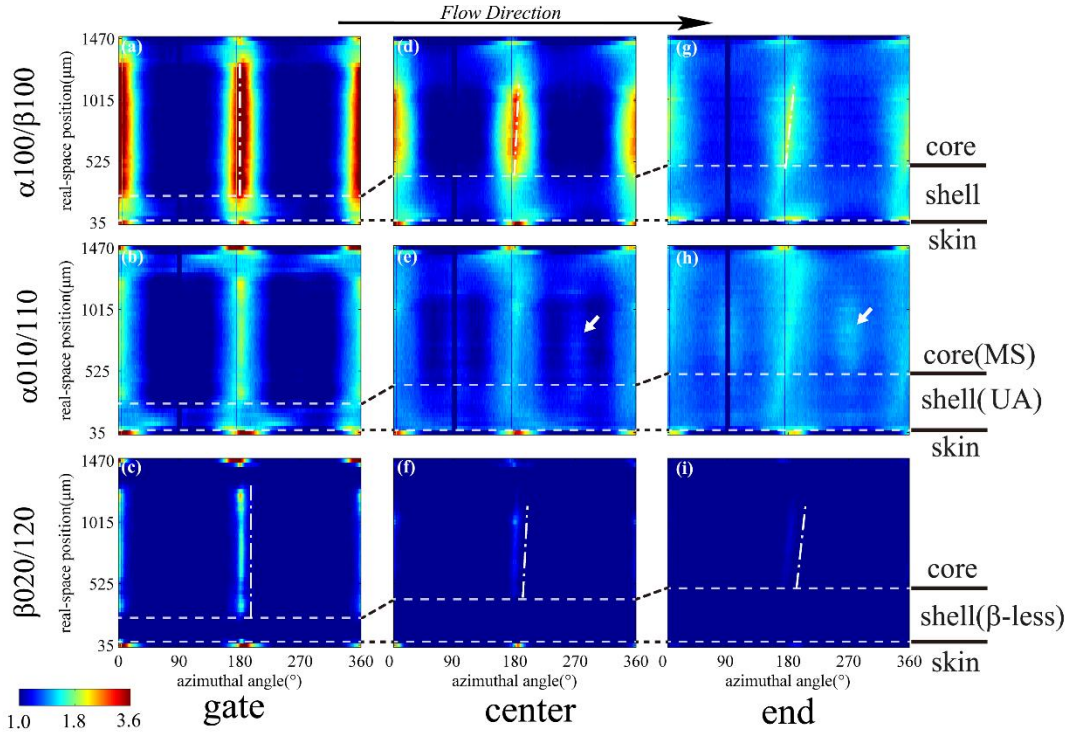

Fig. 6. Normalized azimuthal intensity scans of different reflections (rows) at each position (columns). The rows from the top to the bottom represent the overlapped

α100/β100 reflections (a, d, g), the α010/110 reflections (b, e, h) and the β020/120 reflections at gate position (c, f, i), respectively. The columns from the left to the right represent the reflections at gate (a, b, c), center (d, e, f) and end position (g, h, i), respectively. Note the unequal arcs (UA) and meridian signal (MS) emerging in the α010/110 reflections at different positions. The reduction of color contrast along the FD represents the decreasing of overall orientation.

The skin layer is the strongest oriented layer containing both α-phase and β-phase crystals. The skin layer was only found in the first and last one or two frames. As can be inferred from the reflection maximum off-equatorial shifting, the crystals in this layer show a rotational tilting inward toward the cavity center. The next layer, termed "shell layer", features larger spreads in α100 reflection (Fig. 6a-6c) and arcs with different splitting distance in α010/110 reflections (Fig. 6d-6f).This interesting texture can be attributed to the disorientation and, more prominently, twisting lamellae of the α-phase as mentioned above. Moreover, the most significant characterization of the shell layer can be made by considering the deficiency of β020/120 signals (Fig. 6g-6i). The thickening of the shell layer along the FD can be thus noticed. The core layer, differing markedly from the conventional parts originated from pure shear flow, is uniformly dominated by a highly oriented structure instead of the widely reported large or deformed spherulites.

Another important but often neglected inhomogeneous structure is the structural distribution along the FD. In our case, while the thickness of skin layers remain the same, the reflection signals with both α-phase and β-phase exhibit maxima on about ±7°, ±6°and ±5°to equatorial for the gate, center and end position, respectively. This suggests a non-parallel and varying orientation direction with respect to the FD as mentioned before. The shell layers increase in depth along the LD while core layer narrows down. For those two inner layers, an expected reduction of overall degree of orientation at increasing distance from gate can be observed. However, as can be seen from the shift of reflection maxima (highlighted by white dash dot lines in Fig. 6d-6e and 6g-6h), the crystals of the two inner layers (especially for the shell layer), split by the centerline, tend to tilt outward toward the wall. Notably, this bending direction is totally different from that of skin layer. The maximum tilt degree increases with distance from gate to end but decreases with the distance away from the component surface.

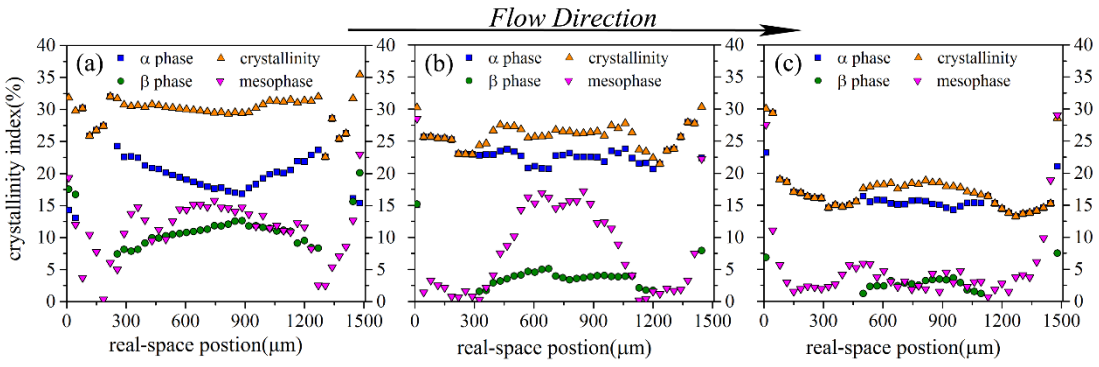

Fig. 7. The crystallinity index as a function of scanning sequence at (a) gate, (b) center, and (c) end. The crystallinity is identified as total (α+β) CI.

The change of phase contents (Fig. 7) again suggests above two anisotropies. The maximum crystallinity is always observed in the skin layer at each position but its magnitude is less obvious at the gate position. The changes of α-phase CI (χ_α) are complicated. For the gate and the center position, the χ_α in the skin layer is lower than that in the shell and core layers, but for the end position the results show the contrary is true. The β-phase CI (χ_β) shows similar distribution through the WD at each position but dramatically decreases with distance from the gate towards the end. The change of mesophase basically follows the trend of the β-phase, which indicates that the β-phase were formed by crystallization of oriented melts and that relaxation of orientation certainly occurs in the shell layer or in the location away from the nozzle entrance. The sharp boundaries between skin-shell-core layers are contrasted by the abrupt changes of χ_β and the percentage of mesophase.

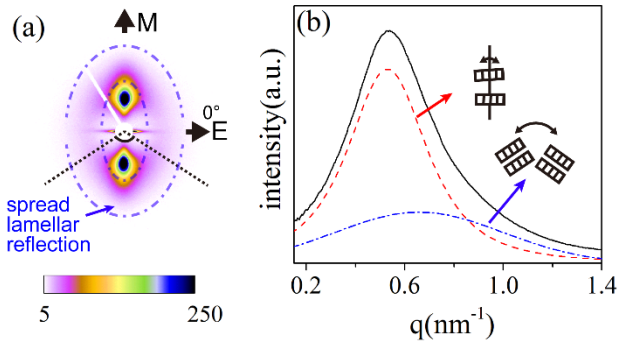

Fig. 8. (a) The SAXS pattern collected at the center position. The spread lamellae reflection was highlighted by the blue dash dot lines. (b) 1D scattering profile of lamellae reflection with integration sector demonstrated by dark dot lines. To exclude

equatorial streak, regions were integrated from -65 ºto -180 º. The cartoon portrays the origin of lamellae reflection in SAXS patterns.

3.4 Molecular origins of anisotropic structure

The SAXS pattern collected at the center position (Fig. 8a) shows an azimuthally narrow equatorial streak and meridian blob-like lamellae reflection. This pattern generally indicates that the presence of oriented shish-kebab structure [27, 41, 42]. Except for those two parts, a rather spread and weak lamellae reflection occurred at larger q can be observed. Figure 8b shows the corresponding lamellae reflection profiles were best fitted by two overlapping peaks. The sharp peak at smaller q is from the lamellar stacks of kebabs [38, 42]. The weak peak belonging to the spread lamellae reflection might be assigned to the "row structure"-those lamellae stacks with smaller long periods and broader orientation distributions [1, 41].

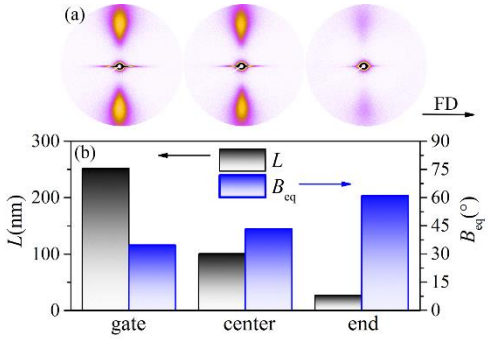

Fig. 9. (a) From left to right, the SAXS patterns at gate, center and end, respectively. (b)The average length of shish-kebabs (L) and integration breadth defining the disorientation degree (B_{eq}) is calculated using $q^2B_{\pi/2}^2(q) = 1/L^2 + q^2B_{eq}^2$, where $B_{\pi/2}(q)$ the integration breadth along azimuthal scan at specific is scattering angle.

Since the beam size used in SAXS experiments is much larger than that in μWAXS, the SAXS patterns should contain aggregated information from different layers. The crystallization morphology in the core layer is represented by shish-kebab structure. This suggestion is based on two above observations: first, the β-phase crystals in the core layer are oriented steadily parallel to the FD and form nuclei from strained melts, which, in smaller structural levels, accords with the fibrous morphology of shish; second, the kebabs themselves could be straight or twisted [38, 43] and possess some degree of freedom to orient with the FD [5], which is only observed in α-phase. It is most possible that the shish backbone consists of β-phase, while continued growth of α-phase forms kebab structures. Mechanically, this conclusion is reconciled when consider the β-phase crystals adopt a less organized alternative sheet stacking arrangement and thus kinetically promote the formation of shish nuclei from oriented melt, while the α-phase crystallize in all sheet stacking progressively, which thermodynamically favors folded-chain lamellae. On the other side, for the shell layer, it is prudent to relate the period system formed by incomplete twisting α-phase crystals to the so-called row structure. Considering the chains and lamellae normals of α-phase crystals are non-parallel, the formation of row structure would be more readily [1].

Since an unexpected core layer structure was observed, it's necessary to quantitatively demonstrate changes of shish-kebab structure in the core layer along

423 the FD. A larger sample-to-detector distance was used to investigate such behavior.
424 Fig. 9a shows the SAXS patterns collected at gate, center and end. The length scale
425 dimension and orientation state of the shish-kebabs are calculated by Ruland's streak
426 fitting method [43-45]. The results in Fig. 9b show that the average length of the
427 shish-kebabs (L) at the gate is around 250 nm but drastically decreases to only 26 nm
428 at the end position. The disorientation degree, represented by values of B_{eq}, gradually
429 increases along the FD. This observation suggests that the shish-kebabs are thin and
430 long-range ordered at the gate while discrete and less oriented one at the end. The
431 average length of shish-kebabs at the end is surprisingly small. However, it might
432 make sense in the case of polyamides. Due to the large decrease in free energy on
433 crystallization as a result of the hydrogen bonding, the long period and lamellae
434 thickness for polyamides is only about 6 ~ 10 nm and 4 nm, respectively. The value of
435 long period is significantly lower than that for polyethylene or polypropylene, which
436 is in the range 18 to 30 nm depending on crystallization condition. The apparent long
437 period at end position is about 10 nm. Morphologically, the scaffold feature of
438 shish-kebab can be satisfied. In fact, the value of 26 nm is very close to the recent
439 result in which the microshish in the initial stage of scaffold-network nuclei was about
440 30 nm [42]. Considering the shish-kebab structures in end position formed under the
441 extensive relaxation condition, the length value of shish would be reasonable.

In addition, two apparent phenomena should also be stressed. One is that the equatorial scattering intensity of center streaks drops faster with distance away from the nozzle entrance, which may be attributed to an increase in interference between the weakly correlated discrete shishes arising from imperfect orientation as well as limited length [46]. The other is that even though the long period of lamellae reflection wouldn't change much, their scattering intensity decreases from gate to end. These two phenomena together indicate that the density of shish-kebabs in the core layer decreases along the FD, which can be confirmed by the WAXS data. Although the WAXS deconvolution results cannot fully represent the structural fraction of larger structures, the relative variations indeed reflect the relaxation of long-range order and loss in average orientation along the FD.

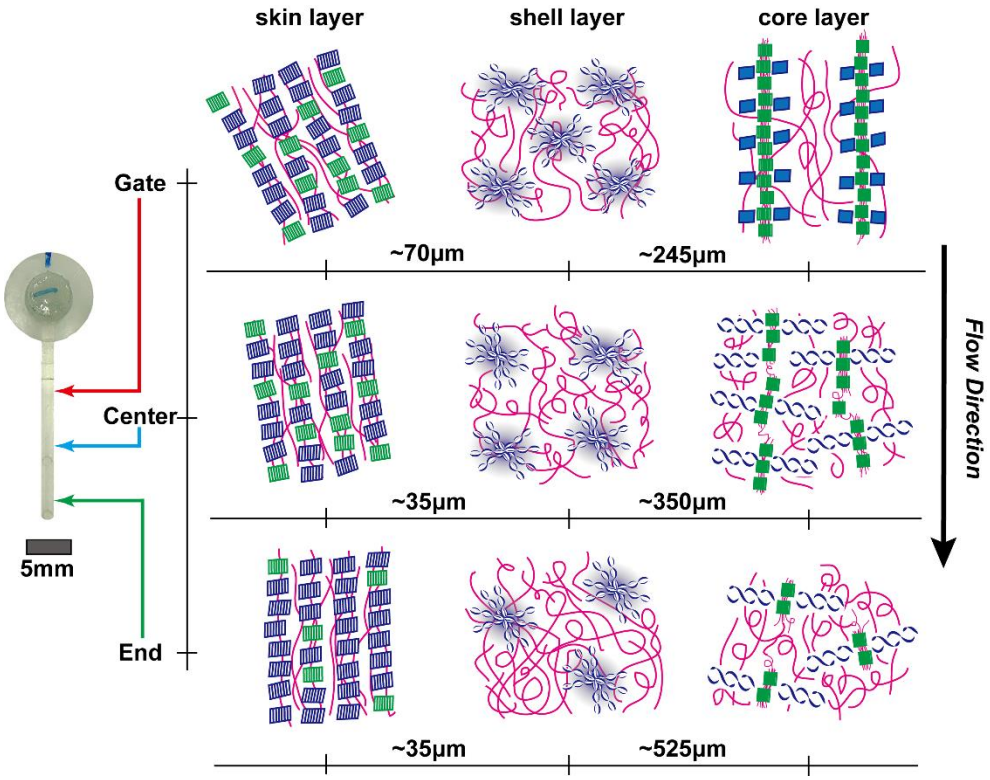

Fig. 10. Schematic illustrations of the crystallization morphology of the skin-shell-core layer structure at different positions within the component. Blue and green stacks represent α-phase crystals and β-phase crystals, respectively. The sheets in β-phase stacks are parallel to lamellae normal while those in straight α-phase stacks are not. The number inside indicate the position of layer border. The scale of lamellae between each layer is not exactly the same.

These analyses declare the observation of novel anisotropic structures of PA1012 under the extensional-shear-coupled flow field Fig. 10 shows the schematic illustration demonstrating the molecular origins of this skin-shell-core layer structure and its evolution along the FD. Nearing the cavity wall, the crystals in the skin layer show a fibrillar texture. The overall (α+β) crystallinity index remains constant along FD. High proportions of mesophase observed in this layer indicate a broad range of high orientation states. Typically, the molecular chain or lamellae normal lie parallel with the surface of the component in the skin layer and that skin layer will narrow down from the gate to end [47]. However, the preferred oriented axis in this case may bend inward to the inner parts at the gate position and become increasingly parallel to cavity surface away from gate position. Moreover, the obvious thinning of the skin layer in common components originated from pure shear geometry cannot be observed, instead, the orientation regularity of lamellae would further increase at the far-end.

Finding no trace of β-phase, the next layer, the shell layer, can thus be recognized. The α-phase crystals in the shell layer exhibit the so-called row structure. This texture can be represented by the relative larger spreads of α-phase reflections and the specific splitting angle of the overlapped α010/110 [39, 41]. Given the contrasts of azimuthal intensity in this layer are still recognizable even at the end position, the existence of isotropic spherulites is denied. The lowest mesophase contents are observed in the shell layer, which means a large number of stretched chains relaxed here. Another notable aspect is that it is observed at the center and end of the component, and that the preferred axis of row structures tends to tilt outward toward the wall (in contrast to the case in the skin layer).

As discussed above, the core layer is characterized by the observation of shish-kebab morphology. The shish is composed of β-phase crystals and, necessarily, of mesophase [44, 48], while the α-phase crystals fall into kebab structures and change from untwisting to complete twisting. The μWAXS and SAXS data together suggest the shish-kebab entities in the core layer shorten in length scale and increase in distribution of orientation along the FD. The evolution of shish-kebabs from gate to end is consistent with the previous investigation [49]: the lower flow rate generates a lower shish density and would enhance the twisting growth of kebabs thereafter.

3.5 Analysis of crystallization dynamics under the complex flow filed

Although the reduction of overall orientation along the FD is expected, it is still interesting to recognize two inverted anisotropic features compared to components originated from pure shear flow geometry. (i) For the skin layer, thinning or loss of orientation cannot be detected. The bending fibrils structure at the gate position gradually becomes parallel to the cavity wall along the FD. Moreover, the orientation regularity increases further at the far-end of the cavity. (ii) The intermediate layer (identified as "shell layer" in this case) is most often characterized by the fine-grained morphology or the shish-kebabs corresponding to different flow or pulse rate rates. While the core layer is isotropic or, at best, deformed spherulites either for macro or micro components [19, 27, 47, 50, 51]. Some special technologies, such as oscillation shear injection molding [50] and gas-assisted injection molding [52] may generate thicker oriented layers, but the regularity that orientation degree consecutively reduces from skin to core remains unchanged. However, a completely opposite is observed in this case: the core layer is dominated by high level of orientation structure whereas the shell layer is not.

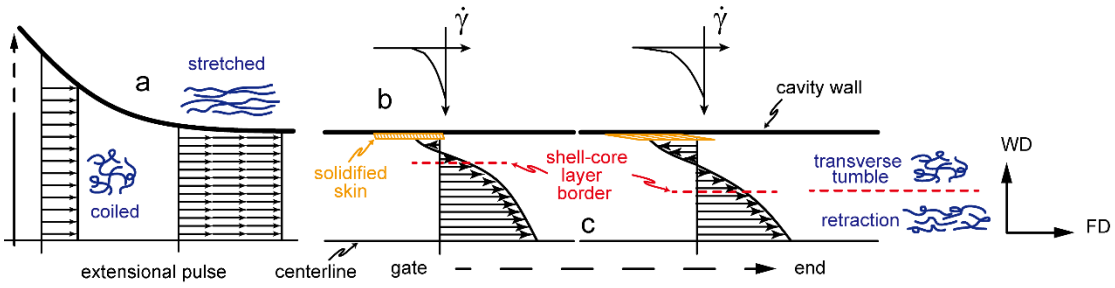

Fig. 11. Schematic illustration of flow condition and its effect on polymer chain sections. (a) Extensional pulse resulting in stretched of HMW tails. (b) Solidified skin

511 is dragged to deform before any debonding occurs. At the end position, strong wall
512 slip results in huge increases in wall shear stress while at the gate position, weak slip
513 only brings about affine deformation. (c) The instantaneous flow geometry of fountain
514 flow in cavity and shear gradient based on previous studies [16-18, 53]. The active
515 area of transverse flow locates near the slip wall where the shear flow emerges. The
516 flow field is separated into two distinguished regions by the red dash lines: the
517 transverse tumble dominant region and retraction dominant region.

518 The unusual anisotropic crystallization morphology of PA1012 cannot be simply
519 interpreted as the consequence of shear-induced crystallization in different flow
520 regime. Due to the strong coupling between extensional flow and shear flow, the flow
521 patterns deviated from pure shear flow. Most importantly, this deviation was recorded
522 owing to the special combination of material and experimental protocol.

523 As discussed before, HMW tails of PA1012 were strongly stretched due to the
524 severe extension effect at the nozzle entrance (Fig. 11a). Once the melt entered into
525 the cavity, considering the mould temperature, 80 ºC, which is close to the glass
526 transition temperature of PA1012, fast solidification (Fig. 11b) would occur at the
527 location near to the cavity wall [54]. However, crystallization was enhanced by the
528 strong stretched polymer chains and, as such, a highly oriented fibrils structure was
529 observed in the skin layer. In addition, because of the high adhesive energy provided
530 by polar amide group, polymer chain of PA1012 would stick to the cavity wall, which

will result in wall slip behavior [55, 56]. The unusual variation trend of the skin layer can be attributed to a "strong-to-weak" wall slip effect [55]. Due to the wall slip effect, the thin skin, with one side being adsorbed to the wall, was dragged by the high-velocity flow elements in the center space of cavity. This effect resulted in bending fibrils structure at the gate, which is much like the affine deformation of a rubber network under an external shear field. A similar texture was observed in a study on gas-assisted injection moulding processing in which the central fluid was high pressure gas [52]. As for the end position, since the fluid elements at this position entered the cavity earlier, a larger magnitude of flow velocity would generate a more strong slip in consequence of debonding of polymer-wall interfacial region [55]. Therefore, more regular and less rotationally tilted fibril crystals were observed.

Since the external characteristic lengths of geometries reduce enormously compared to the ideal condition, laminar flow would not fully develop after the rapidly extensional pulse. The implication is that the flow behavior would be more close to a "global" fountain flow. The fountain effect for polymer generates a localized hydrodynamic phenomenon demonstrated by the complex two-dimensional flow (axial and transverse) [16, 57, 58]. Question on whether fountain flow influences the molecular orientation still remains nowadays [59, 60]. Fig. 11c shows the instantaneous flow profile of the fountain flow at the end and gate positions in which fluid elements between the centerline and slip interface would decelerate in the

direction of flow and would acquire a transverse velocity spilling outward toward the wall [16, 53, 57]. According to the chain behavior proposed by Chu et al [38, 61, 62], this transverse velocity perpendicular to the flow could bring about hydrodynamic drag forces and tumble effect to coil the stretched chains at an intermediate region near to the wall, for which relaxation might be accelerated. It is most possible that the fast relaxation caused by tumble effect lead to the formation of twisting row structure in the shell layer, since this kind of period structure is favored under intermediate strain condition [1]. Referring to the thickness of shell layer, the transvers tumble dominant regions are identified. As highlighted by the red dotted line, the maximum transverse velocity located on the side nearing to slip wall and its active area would be largest at flow front [16, 57]. Considering that, it is convenient to understand the sharp shell-core layer border. The higher and wider-area transverse flow at the flow front results in the thicker and less oriented shell layer at end position, and notably, the larger tilt of crystals in the shell layer as well as part of the core layer at the far end will be observed.

Although the magnitude of the transverse velocity is much smaller around the centerline, the stretch chains in this region would get through continuous retraction. However, in our case, reconstruction of hydrogen bonding between polymer chains slowed the retraction process of stretched HMW tails, which was enough for the development of shish nuclei in core layer. On the other side, the morphological

differences of kebab in core layer could clearly distinguish the different relaxation degree along the FD [38, 49]. One should notice that, even though extensional pulse was sufficiently strong and PA 1012 solidified rapidly, a dramatic decrease of density and length of shish at the center and end position could be observed. This suggests, for most cases, the effect of extensional pulse on the polymer melt would be restrained and further diminished along the FD. Hence, it is also very important to know that no observable trend of deformation and orientation phase in core layer means zero-stress boundary in the centerline of cavity but does not necessarily mean nothing happens there.

4. Conclusions

A special combination of experimental protocols and polymer system was presented for investigating the flow-induced crystallization of polymer melts under the complex flow field. The line-scan collections of synchrotron μWAXS at three different positions of final component provide a clue to comprehensively assess the crystallization textures and flow behavior of polymer melts. The crystallization structure, multiple orientation and phase contents together indicate a novel inverted anisotropic structure: along the FD, a skin layer showing more regular and less rotational tilted orientation at the far-end of the cavity; perpendicular to the flow, the shell layer showing less oriented twisting row structures consisted of α-phase crystals only, while the core layer showing shish-kebabs for which the complete twisting

591 α-phase lamellae epitaxially growing on the β-phase shish. These textures were
592 confirmed by small-angle X-ray scattering. The inverted layer structure implies the
593 wall slip and a global fountain flow happened under the complex flow field. Certain
594 question was stressed on whether the fountain flow influences the molecular
595 orientation. The answer seems to be that the fountain flow itself would not enhance
596 the molecular orientation. On the contrary, if polymer chains are sufficiently extended,
597 the transverse tumble of fountain flow would speed up the retraction of oriented
598 chains in intermediate region between skin and core. The quantitative analysis on the
599 shish-kebabs in the core layer suggests the effect of extensional pulse should be
600 valued in the small-scaled geometries or under the high strain rate condition.

601 **Acknowledgements**

602 We would like to thank the generous financial support by following grants: R&D
603 Program of the Ministry of Science and Technology (2013BAE02B02), National
604 Natural Sciences Foundation of China (51173195) and Strategic Priority Research
605 Program of the Chinese Academy of Sciences (XDA01020304). We also thank the
606 beam times on BL15U, BL14B1 and BL16B1 in SSRF of China.

607

608 **References**

609 [1] Keller A, Machin MJ. J Macromol Sci Part B Phys 1967;1(1):41-91.
610 [2] Kumaraswamy G, Issaian AM, Kornfield JA. Macromolecules 1999;32(22):7537-47.
611 [3] Somani RH, Hsiao BS, Nogales A, Srinivas S, Tsou AH, Sics I, Balta-Calleja FJ,
612 Ezquerra TA. Macromolecules 2000;33(25):9385-94.

[4] Somani RH, Hsiao BS, Nogales A, Fruitwala H, Srinivas S, Tsou AH. Macromolecules 2001;34(17):5902-09.
[5] Li L, de Jeu W. Flow-induced mesophases in crystallizable polymers. Interphases and Mesophases in Polymer Crystallization II, vol. 181: Springer Berlin Heidelberg, 2005. pp. 75-120.
[6] Liedauer S, Eder G, Janeschitz-Kriegl H, Jerschow P, Geymayer W, Ingolic E. Int Polym Proc 1993;8(3):236-44.
[7] Ratajski E, Janeschitz-Kriegl H. Polym Bull 2012;68(6):1723-30.
[8] Duplay C, Monasse B, Haudin JM, Costa JL. J Mater Sci 2000;35(24):6093-103.
[9] Cui K, Meng L, Ji Y, Li J, Zhu S, Li X, Tian N, Liu D, Li L. Macromolecules 2014;47(2):677-86.
[10] Cogswell FN. J Rheol 1972;16(3):383-403.
[11] Bischoff White E, Henning Winter H, Rothstein J. Rheol Acta 2012;51(4):303-14.
[12] Bushman AC, McHugh AJ. J Appl Polym Sci 1997;64(11):2165-76.
[13] Stadlbauer M, Janeschitz-Kriegl H, Eder G, Ratajski E. J Rheol 2004;48(3):631-39.
[14] Graham RS. Chem Commun 2014;50(27):3531-45.
[15] Gogos CG, Huang C-F, Schmidt LR. Polym Eng Sci 1986;26(20):1457-66.
[16] Mavridis H, Hrymak AN, Vlachopoulos J. J Rheol 1988;32(6):639-63.
[17] Bensaad S, Jasse B, Noel C. Polymer 1999;40(26):7295-301.
[18] Patham B, Papworth P, Jayaraman K, Shu C, Wolkowicz MD. J Appl Polym Sci 2005;96(2):423-34.
[19] van Meerveld J, Peters GM, Hütter M. Rheol Acta 2004;44(2):119-34.
[20] Jeong J-H, Leonov AI. Polym Eng Sci 2008;48(12):2340-53.
[21] Whiteside BR, Martyn MT, Coates PD, Greenway G, Allen P, Hornsby P. Plast Rubber Compos 2004;33(1):11-17.
[22] Whiteside BR, Spares R, Brown EC, Norris K, Coates PD, Kobayashi M, Jen CK, Cheng CC. Plast Rubber Compos 2008;37(2-4):57-66.
[23] Boussia AC, Vouyiouka SN, Porfiris AD, Papaspyrides CD. Macromol Mater Eng 2010;295(9):812-21.
[24] Seguela R. J Macromol Sc. Part C Poly R 2005;45(3):263-87.
[25] Zafeiropoulos NE, Davies RJ, Roth SV, Burghammer M, Schneider K, Riekel C, Stamm M. Macromol Rapid Commun 2005;26(19):1547-51.
[26] Davies RJ, Burghammer M, Riekel C. Macromolecules 2007;40(14):5038-46.
[27] Schrauwen BAG, Breemen LCAv, Spoelstra AB, Govaert LE, Peters GWM, Meijer HEH. Macromolecules 2004;37(23):8618-33.
[28] Wu J, Schultz JM. Polymer 2002;43(25):6695-700.
[29] Dealy JM. Rheol Bull 2010;79(2):14-18.
[30] Zhong Y, Fang H, Zhang Y, Wang Z, Yang J, Wang Z. ACS Sust Chem Eng 2013;1(6):663-72.
[31] Doi M, Edwards SF. The Theory of Polymer Dynamics: Clarendon Press: Oxford, 1986.

[32] Hou J-X, Svaneborg C, Everaers R, Grest GS. Phys Rev Lett 2010;105(6):068301.
[33] Hsiao BS, Kennedy AD, Leach RA, Chu B, Harney P. J Appl Crystallogr 1997;30(6):1084-95.
[34] Lotz, B, Cheng, SZD Polymer 2005; 46(3): 577-610.
[35] Jones Na, Atkins EDT, Hill MJ, Cooper SJ, Franco L. Polymer 1997;38(11):2689-99.
[36] Jones NA, Atkins EDT, Hill MJ, Cooper SJ, Franco L. Macromolecules 1997;30(12):3569-78.
[37] Dreyfuss P, Keller A. J Macromol Sci Part B 1970;4(4):811-35.
[38] Somani RH, Yang L, Zhu L, Hsiao BS. Polymer 2005;46(20):8587-623.
[39] Feldman AY, Fernanda Gonzalez M, Wachtel E, Moret MP, Marom G. Polymer 2004;45(21):7239-45.
[40] Jerschow P, Janeschitz-Kriegl H. Rheol Acta 1996;35(2):127-33.
[41] Wu J, Schultz JM, Yeh F, Hsiao BS, Chu B. Macromolecules 2000;33(5):1765-77.
[42] Liu D, Tian N, Cui K, Zhou W, Li X, Li L. Macromolecules 2013;46(9):3435-43.
[43] Yang L, Somani RH, Sics I, Hsiao BS, Kolb R, Fruitwala H, Ong C. Macromolecules 2004;37(13):4845-59.
[44] Hsiao BS, Yang L, Somani RH, Avila-Orta CA, Zhu L. Phys Rev Lett 2005;94(11):117802.
[45] Thünemann AF, Ruland W. Macromolecules 2000;33(5):1848-52.
[46] Murthy NS, Bednarczyk C, Moore RAF, Grubb DT. J Polym Sci Poly Phys 1996;34(5):821-34.
[47] Katti SS, Schultz M. Polym Eng Sci 1982;22(16):1001-17.
[48] Kimata S, Sakurai T, Nozue Y, Kasahara T, Yamaguchi N, Karino T, Shibayama M, Kornfield JA. Science 2007;316(5827):1014-17.
[49] Keum JK, Burger C, Zuo F, Hsiao BS. Polymer 2007;48(15):4511-19.
[50] Yang H-R, Lei J, Li L, Fu Q, Li Z-M. Macromolecules 2012;45(16):6600-10.
[51] Lin X, Caton-Rose F, Ren D, Wang K, Coates P. J Polym Res 2013;20(4):1-12.
[52] Wang L, Wang JH, Yang B, Wang Y, Zhang QP, Yang MB, Feng JM. Colloid Polym Sci 2013;291(6):1503-11.
[53] Lee H-S. Polym Eng Sci 1997;37(3):559-67.
[54] Fitchmun DR, Mencik Z. J Polym Sci Poly Phys 1973;11(5):951-71.
[55] Joshi YM, Lele AK, Mashelkar RA. J Non-Newtonian Fluid Mech 2000;94(2–3):135-49.
[56] Boukany PE, Wang S-Q. Macromolecules 2009;42(6):2222-28.
[57] Coyle DJ, Blake JW, Macosko CW. AlChE J 1987;33(7):1168-77.
[58] Hsiung CM, Cakmak M, Ulcer Y. Polymer 1996;37(20):4555-71.
[59] Nguyen-Chung T, Mennig G. Plast Rubber Compos 2006;35(10):418-24.
[60] Kobayashi Y, Otsuki Y, Kanai T. Polym Eng Sci 2010;50(11):2182-89.
[61] Somani RH, Yang L, Hsiao BS, Sun T, Pogodina NV, Lustiger A. Macromolecules 2005;38(4):1244-55.
[62] Smith DE, Babcock HP, Chu S. Science 1999;283(5408):1724-27

695